Confined spin waves in magnetochiral nanotubes with axial and circumferential magnetization

Maria Carmen Giordano ⊙, Mohammad Hamdi ⊙, and Andrea Mucchietto⊙

École Polytechnique Fédérale de Lausanne (EPFL), School of Engineering, Institute of Materials, Laboratory of Nanoscale Magnetic
Materials and Magnonics, 1015 Lausanne, Switzerland

Dirk Grundler ⊙[*]

École Polytechnique Fédérale de Lausanne (EPFL), School of Engineering, Institute of Materials, Laboratory of Nanoscale Magnetic
Materials and Magnonics, 1015 Lausanne, Switzerland
and École Polytechnique Fédérale de Lausanne, School of Engineering, Institute of Electrical and Micro Engineering,
1015 Lausanne, Switzerland

We report experimental studies of spin-wave excitations in individual 22-nm-thick $Ni_{80}Fe_{20}$ nanotubes with diameters of about 150 nm. We apply Brillouin light-scattering spectroscopy under microwave irradiation, and we resolve sets of discrete resonances in the center of nanotubes ranging from 2.5 to 12.5 GHz. Comparing to a recent theoretical work and micromagnetic simulations, we identify different characteristic eigenmodes depending on the axial, mixed, or vortex configuration. The mixed and vortex states give rise to modes with helical phase profiles substantiating an unusual nature of confined modes attributed to nonreciprocal spin waves. Our findings provide microscopic insight into realistic tubular spin-wave nanocavities and magnetochiral effects for three-dimensional nanomagnonics.

I. INTRODUCTION

Advances in magnonics foster new ideas for information processing based on reciprocal and nonreciprocal short-wave magnons [1–3]. They set novel grounds for logic nanoelements which, not relying on charge transport, have the advantage of operating with low-energy consumption. Among these elements, three-dimensional (3D) magnetic nanostructures are very promising for achieving high integration density [3–6]. Their potential will materialize only when the underlying spin dynamics is understood [7–9].

Nanotubes (NTs) prepared from ferromagnets represent prototypical 3D nanomagnetic structures [9]. They are extremely versatile as their properties change as a function of both their geometrical parameters (namely length, inner radius, and outer radius [10–12]) and their axial, helical, or vortexlike magnetic configuration [13,14]. A curvature-induced magnetochiral field originates from dipole-dipole interaction [15] and can induce nonreciprocal spin-wave dispersion relations in the case of cylindrical NTs with nanometric radii and circular cross sections [8,14,16–18]. Previous experimental studies based on microtubes prepared from rolled-up ferromagnetic layers [19,20] have not addressed magnetochiral effects as radii were in the micrometer regime. Ferromagnetic nanotubes were investigated recently, however, with hexagonal cross sections [13,21–24]. In axially magnetized NTs prepared from magnetically isotropic Ni, a series of spin-wave resonances were resolved and classified depending on the number of assumed nodal lines in the

azimuthal direction [21]. The phase distribution across the NTs as explored theoretically in Refs. [18,24] was not discussed. Koerber *et al.* [23] studied propagating spin waves along a $Ni_{80}Fe_{20}$ (permalloy) NT, and they reported the asymmetric spin-wave transport originally predicted for the cylindrical NTs. Here, the vortex configuration was induced via a growth-induced magnetic anisotropy and not by the dipolar interaction relevant for the curvature-induced nonreciprocity. For the simulations, the authors considered an ideal hexagonal nanotube. They did not take into account symmetry-breaking aspects such as slanted end surfaces [25] or vortexlike segments of opposing chirality [26], which occur in real nanotubes. Short-segmented nanotubes might serve as vertical through-chip vias in 3D magnonic device architecture [27].

Here, we investigate spin-wave modes in NTs with a hexagonal cross section prepared from permalloy (Py) grown by a recently developed plasma-enhanced atomic layer deposition (PEALD) process [22,28]. Combining Brillouin light scattering (BLS) microscopy [Fig. 1(a)] and micromagnetic simulations, we explore the nature of modes occurring in different magnetic configurations with and without helically magnetized segments. Depending on the applied magnetic field, we resolve a multitude of spin-wave branches consistent with performed micromagnetic simulations. The latter ones consider symmetry-breaking irregularities of a real nanotube, and they allow us to relate simulated spin-wave modes with helical phase patterns to the measured branches. The phase patterns substantiate a curvature-induced magnetochiral effect that was predicted first for circular NTs and then for hexagonal cross sections [24]. We find an unusual nature of confined modes, which so far has been restricted to magnets with
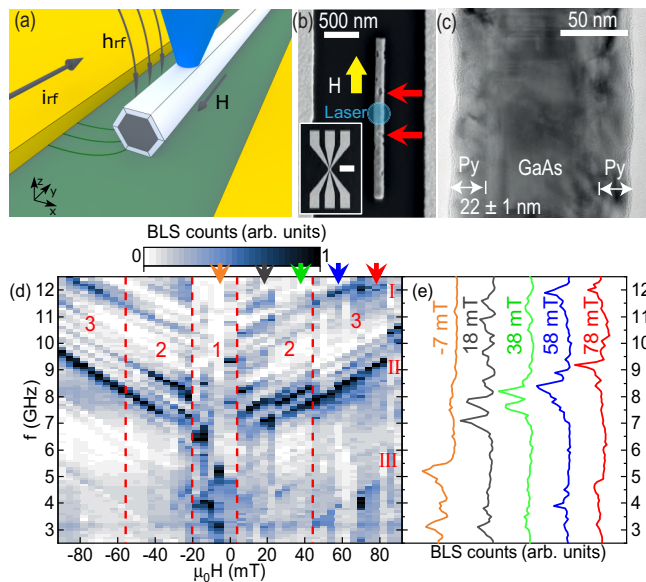
---

[*]dirk.grundler@epfl.ch

FIG. 1. (a) Sketched excitation-detection scheme based on a coplanar wave guide (CPW) and microfocus Brillouin light scattering microscopy. (b) Scanning electron microscopy image of the nanotube placed parallel to the CPW. The red arrows indicate the nanothroughs (inset: CPW at a smaller magnification; scale bar: 200 μm). (c) Transmission electron microscopy image of a Py nanotube on a GaAs core. Shell thickness: 22 ± 1 nm. (d) BLS spectra detected at room temperature at the NT center as a function of field H applied along the NT axis. Colored arrows indicate fields -7, 18, 38, 58, and 78 mT at which we extract (e) line spectra.

Dzyaloshinskii-Moriya interaction [29,30] and which puts a new spin on 3D nanomagnonics.

II. METHODS

A. Microfocus Brillouin light scattering

The experiments are based on NTs that are positioned in the gap of a coplanar waveguide (CPW) [Fig. 1(a)]. The NTs were obtained through conformal coating of hexagonal semiconductor nanowires (for further details, see the supplemental material [31] and Refs. [32,33]). The regular hexagonal cross-section of the nanotemplate covered with a conformal ferromagnetic shell can be seen in supplementary Fig. S1 (Fig. 1) of Ref. [21] (Ref. [34]). Preliminary magnetization dynamics measurements on films and NTs [22] have shown that the PEALD-grown Py showed a low damping and was magnetically isotropic. Our NTs, therefore, exhibit a different effective field compared to Ref. [23]. An rf-current i_{rf} applied to the CPW generates a dynamic magnetic field h_{rf}. h_{rf} excites spin precession in the adjacent ferromagnetic NT [Fig. 1(b)] at the given frequency f. Spin-precessional motion is detected for different f varied from 2.5 to 12.5 GHz using BLS microscopy (μ-BLS) [35,36] at room temperature. To detect the microwave-stimulated magnon resonances locally, we focus a monochromatic blue laser on the sample's top surface and collect the inelastically scattered light in back-reflection geometry. At a laser wavelength of 473 nm, the penetration depth in Py amounts to about 10 nm. Hence the BLS is more sensitive to modes localized on the outer surface.

The investigated samples consist of a 22-nm-thick Py shell covering a hexagonal GaAs nanowire core and a 5 nm thin spacer layer of Al_2O_3 used to separate Py and GaAs. In Fig. 1(c) a transmission electron micrograph of the cross section of a NT from the same batch is shown. For the NT upon which we focus here, we estimate the effective outer radius to be $r_o = 80$ nm and the inner radius to be $r_i = 58$ nm according to Refs. [21,28] (results on a further NT are presented in the supplemental material [31]). An external magnetic field H is applied along the NT axis (**z**-direction). The position of the BLS laser spot is marked with a blue circle in Fig. 1(b), which is comparable to the diameter of the real laser (about 400 nm). It is positioned in the center of the NT between two nanotroughs which are separated by 560 nm. In our experiments, these nanotroughs are expected to operate as microwave-irradiated emitters of short-wave magnons [37].

B. Micromagnetic simulations and comparison with experimental spectra

Micromagnetic simulations have been performed using OOMMF [38] with parameters reported in the supplemental material [31]. They provided us with eigenfrequencies extracted from power spectral density (PSD) spectra and spin-precessional motion visualized using Mayavi [39] (see also the videos in the supplemental material [31]). We do not compare simulated and measured signal strengths quantitatively. The magnetic pulse in micromagnetic simulations is homogeneous in space, while the field of the CPW is inhomogeneous. This discrepancy makes signal strengths different. The finite penetration depth of the laser is not considered in the simulations. This experimental feature modifies the signal strengths of different modes. It might obscure weak modes and bury them in the finite noise level of the experimental setup. Overall, we expect to detect experimentally the modes with a different amplitude distribution than simulated. Some modes might be missing in the measured spectra. In Ref. [24] a theoretical work is presented that provides further details of modes that occur in long nanotubes with different magnetization configurations.

III. FIELD DEPENDENCY OF SPIN-WAVE SPECTRA

In Fig. 1(d) (Fig. S3) we show the field-dependent BLS spectra detected for sample NT-s1 (NT-s2) under microwave irradiation for which we varied the frequency between 2.5 and 12.5 GHz. The data were acquired for static fields $\mu_0 H$ changing from $+90$ to -90 mT. To display them, we use the scientific color maps developed by Crameri *et al.* [40] and prevent visual distortion of the data and exclusion of readers with color-vision deficiencies [41]. Colored arrows on the top indicate the specific fields for which spectra are displayed in Fig. 1(e). Several branches of distinguished eigenmodes are resolved. The Py NTs investigated here show richer spectra compared to the recently studied Ni NTs [21]. We attribute this observation to the improved damping parameter $\alpha_{Py} = 0.013$ of the PEALD-grown Py [22] compared to $\alpha_{Ni} = 0.045$

for PEALD-grown Ni [28]. The spectra reported here are also richer compared to Py disks [42] and Py rings [43].

The main identified resonance modes show nearly linear dependencies of f on H for $|\mu_0 H| \geqslant 42$ mT, i.e., in field regime 3 of Fig. 1(d). We categorize the observed branches in three groups I, II, and III by which we subdivide the frequency regime from 2.5 to 12.5 GHz into three parts. When reducing the field below $+42$ mT, we notice an increase of intensity (dark color) for certain branches near 8 GHz (group II), suggesting a change in the magnetic configuration when entering field regime 2. Similar behavior is observed for the spectra detected in the regime 2 at negative magnetic fields. In field regime 1 at negative fields, strong resonances (dark color) occur at low f down to about 2.5 GHz and at large f of about 9 GHz. Together with the lack of mirror symmetry with respect to $\mu_0 H = 0$, these resonances indicate the irreversible reversal process of the nanotube near $H = 0$.

Our simulations (shown in the supplemental material) indicate that a vortex configuration is formed near zero field. The low resonance frequencies in regime 1 are consistent with such a magnetic state. Considering the pronounced intensity of branches near 8 GHz in regime 2, a large part of the NT exhibits a reversed magnetization at -18 mT when coming from positive H. In Ref. [14], the authors predicted small (large) resonance frequencies for nonreciprocal spin waves in a vortex (axial) magnetic configuration of a circular NT at zero (large) magnetic field, in agreement with the frequency variation of branches observed in Fig. 1(d).

IV. SPIN-WAVE CONFINEMENT AND MAGNETIC CONFIGURATIONS IN A REAL NANOTUBE

The richness of the spectra and the resonant modes in group III at large H in Figs. 1(d) and S3 suggest that not only azimuthal, but also longitudinal confinement is relevant. For the latter aspect, it is reasonable to assume that the nanotroughs in the NTs either provide confining boundaries like antidots [44] or act as spin-wave emitters that are coherently excited by the global microwave field of the CPW [37] and thereby induce interference patterns (standing spin waves) between pairs of nanotroughs [45]. These assumptions motivated us to perform simulations on an irregularly defined NT segment instead of an infinitely long NT as was done previously. We hence performed simulations of an (approximately) 560-nm-long hexagonal nanotube with slanted edges [31]. These end facets were not parallel and designed such that the finite-sized NT segment had slightly different lengths L' and L'' on different sides ($L' > L''$). With the help of the static micromagnetic simulations (shown in Fig. S4) we attribute the field regions 1, 2, and 3 to three distinctly different configurations of the NT magnetization $\mathbf{M}$. Coming from large positive H, simulations predict an axial (saturated) state (region 3), and a mixed state without (region 2) and with (region 1) a Néel-type domain wall (DW), respectively. In regions 2 and 1, parts of the NTs are in a helical magnetic configuration. In the following, we compare dynamic simulations in different regions to experimental BLS spectra, and we report the emergence of helical spin-wave modes.
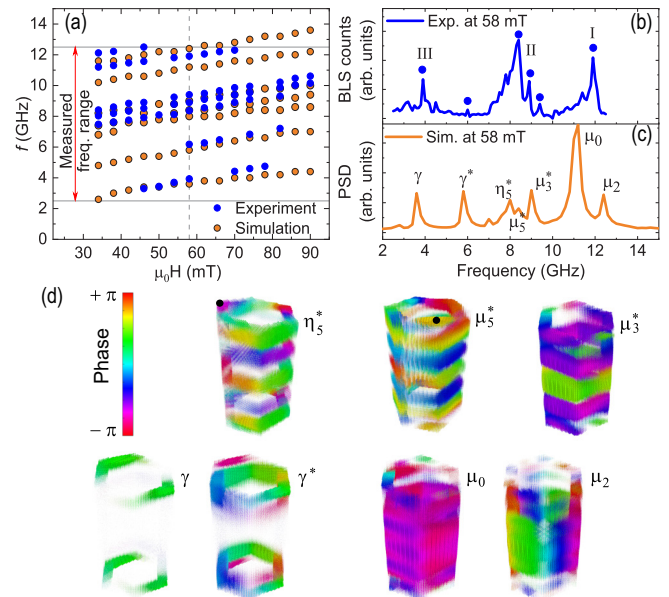

FIG. 2. (a) Eigenmode frequencies detected by μBLS in the central part of a Py NT (blue circles) and simulated resonance frequencies (orange circles) plotted as a function of the magnetic field inducing an axial magnetic state. (b) BLS spectrum and (c) simulated spectrum obtained for a field of 58 mT. Principal eigenmodes are labeled by different letters and correspond to dynamic magnetization profiles in (d). The size of the dots represents the amplitude. The color bar represents spin-wave phase ranging from $-\pi$ to $+\pi$.

A. Spin waves in the axially magnetized configuration

It is instructive to first discuss the axial state at large positive fields. In our analysis, we consider prominent peaks and the frequency regime between 2.5 and 12.5 GHz covered by the BLS experiment. In Fig. 2(a) we summarize resonance frequencies extracted from μ-BLS between nanotroughs of Py NT-s1 (blue circles) and the simulated resonance frequencies (orange circles) plotted as a function of H. Experimentally determined resonance frequencies match well with simulated ones (see also Fig. S5). Representative spectra are displayed for 58 mT in Figs. 2(b) and 2(c) for the experiment and the simulation, respectively. In Fig. 2(b), labels I, II, and III are according to the groups of resonances defined in Fig. 1(d). In Fig. 2(c), the Greek symbols refer to the dynamic magnetization profiles (mode patterns) shown in Fig. 1(d), which are representative for all the fields of the axial (saturated) magnetic state. In the following, we discuss the frequency values of resonant modes, and we do not refer to the predicted intensities as the selectivity of the BLS microscope concerning specific mode patterns has not been simulated. We follow the nomenclature for modes introduced in Ref. [46]. Simulated modes μ_0 and μ_2 occurring at 11.2 and 12.4 GHz, respectively, belong to group I. The mode profile μ_0 [Fig. 2(d) and supplemental movie1 in the supplemental material [31]] corresponds to an in-phase spin precession, which is nearly uniform across the NT and can be considered as the ferromagnetic resonance (FMR) with a total wave vector $k = \sqrt{k_z^2 + k_\varphi^2} = 0$, where $\mathbf{k}_z$ ($\mathbf{k}_\varphi$) denote wave vectors in the $\mathbf{z}$ (azimuthal) direction [14]. For spin waves with nonzero

wave vector, the finite length and circumference of the nanotube impose a quantization condition on k_z and k_φ, respectively. The quantization condition for k_z (k_φ) reads $k_z = k_{z,m} = m\pi/L$ ($k_\varphi = k_{\varphi,\nu} = \nu \times 2\pi/C$). We therefore rewrite the total wave vector $\mathbf{k} = \mathbf{k}_{m\nu} = \mathbf{k}_{z,m} + \mathbf{k}_{\varphi,\nu}$. The mode μ_2 illustrates an azimuthal spin wave (supplemental movie2 [31]) with total wave vector k_{02}, i.e., $k_z = 0$ and $k_\varphi = 2 \times 2\pi/C = 26.2$ rad/µm. ν counts the periods in the azimuthal (φ) direction [24]. $C = 480$ nm is the circumference of the hexagonal NT as defined in Ref. [21]. Considering $\mathbf{k}_\varphi \perp \mathbf{M}$, the mode reflects the Damon-Eshbach (DE) configuration. Consistent with Ref. [24], its frequency is larger than the FMR. We note that clockwise and counterclockwise azimuthal modes with $\nu \neq 0$ are split in eigenfrequency by the topological Aharonov-Bohm effect, and a standing wave is not formed in the azimuthal direction [18,24].

Simulated modes labeled as μ_3^*, μ_5^*, and η_5^* have eigenfrequencies of 9, 8.4, and 8 GHz, respectively, consistent with group II resonances. The mode profile of μ_3^* agrees with a standing wave confined along a fixed length L, i.e., $k_{m\nu} = k_{m0}$, with a nonzero $k_z = m\pi/L$, where $m = 1, 2, \ldots$ and $\nu = 0$. In this case, $\mathbf{k}_z$ is parallel to $\mathbf{M}$ consistent with a backward volume magnetostatic spin wave (BVMSW) configuration. Such modes do not have a pronounced nonreciprocity in axially magnetized NTs [14]. Hence in Fig. 2(d) (see supplemental movie3 [31]), the profile μ_3^* incorporates two nearly parallel nodal lines. In Fig. 2(d), the mode profiles of μ_5^* and η_5^* are rotated to position in each case the facet with the predominant spin-precessional amplitude on the right side (the profile of η_5^* was rotated by 120° anticlockwise around the $\mathbf{z}$-axis with respect to the profile of μ_5^*). The same corners are marked with black circles. We find that the mode profiles μ_5^* and η_5^* represent standing waves with $m = 5$ confined along facets of different lengths L' and L'', respectively (see supplemental movie4 and movie5 [31]). The different longitudinal confinement explains the discrepancy in frequency. The modes labeled γ and γ^* belong to group III with resonant frequencies 3.6 and 5.8 GHz, respectively (see supplemental movie6 and movie7 [31]). Here, spin precession occurs right at the NT edges. Such edge modes [47] have the lowest frequencies due to the demagnetizing effect and small internal fields at edges and the nanotroughs [48]. The fundamental and first higher-order edge mode with larger k_z are separated by about 2.2 GHz, which we attribute mainly to exchange interaction.

B. Spin waves in the mixed state with end vortices

As H is reduced, the mixed state is formed with magnetization vortices of opposite chirality at the ends of the simulated NT and neighboring helically aligned segments [Fig. 3(a)]. Following Ref. [14], NT segments with a circumferential, i.e., helical (vortex) magnetic configuration support nonreciprocal spin waves for nonzero k (k_z). This nonreciprocity has the same origin as in the case of the azimuthal modes in the longitudinally saturated state, i.e., the localization of DE-type modes on either the inner or the outer nanotube surface where demagnetizing dynamic fields differ because of different curvatures. The measured (simulated) spectrum at zero field is shown in Fig. 3(b) [Fig. 3(c)]. Simulated phase distributions are shown in Fig. 3(d). Mode h_α shown in
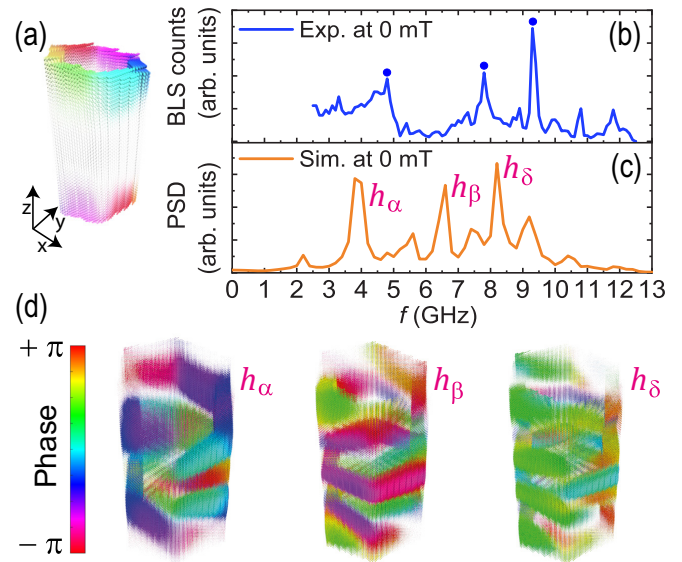

FIG. 3. (a) Simulated static magnetization profile of the NT at $\mu_0 H_z = 0$ mT. (b) NT-s1 BLS spectrum and (c) simulated spectrum at 0 mT. Specific eigenmodes are labeled by h_α, h_β, and h_δ and tentatively attributed to modes marked by dots in (b). (d) Dynamic magnetization profiles of modes defined in (c). The size of the dots represents the amplitude. The color bar represents spin-wave phase ranging from $-\pi$ to $+\pi$.

Fig. 3(d) (supplemental movie8 [31]) derives most probably from the low-frequency edge mode discussed before. When extending into the helically aligned center region, the mode exhibits a complex helical phase pattern as nonreciprocal spin waves cannot form the regular standing-wave patterns [29]. Modes h_β and h_δ (see supplemental movie9 and movie10 [31]) reside at higher f suggesting a larger k_z. Different from mode μ_3^* of the axially aligned state, regular phase patterns with nearly parallel nodal lines are not retrieved in the helical state.

Comparing simulated and experimental spectra in Figs. 2 and 3, we observe an overall discrepancy of approximately 1 GHz between prominent peaks in measured (indicated by dots) and simulated (indicated by labels) spectra. We explain the discrepancy with the geometry of the real NT, which extends beyond the nanotroughs, leading to an overall smaller demagnetization effect compared to the simulated NT. The latter one has hence a smaller internal field, i.e., smaller eigenfrequencies [48] than the measured NT.

C. Spin waves in the mixed state incorporating a central domain wall

We now discuss spin waves in the mixed state at $\mu_0 H_z = -14$ mT in which a central DW is assumed [Fig. 4(a)]. The simulation shows two end vortices of opposite chirality that extend to the center. Their circumferential magnetization configurations meet in a Néel-type DW (white region). The detected BLS spectrum at -14 mT is reported in Fig. 4(b) and contains at least three groups of peaks near 4, 6.5, and 8.5 GHz. In the simulated spectrum [Fig. 4(c)] also different groups are identified, which we label by d, m, and
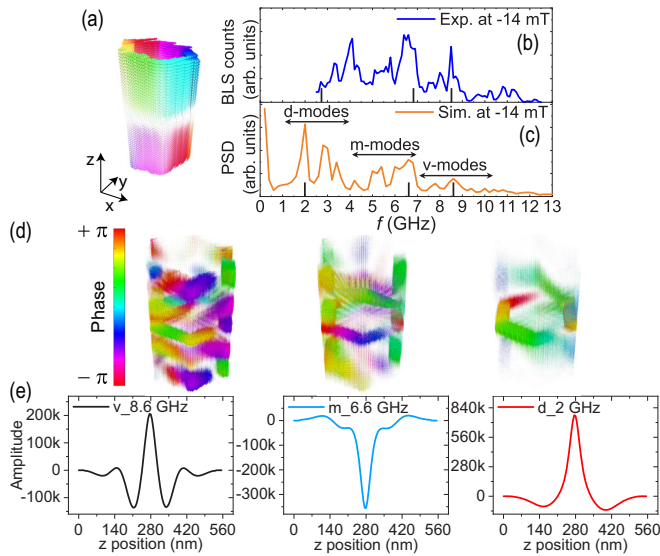
FIG. 4. (a) Simulated static magnetization profile of the NT at $\mu_0 H_z = -14$ mT. (b) BLS and (c) simulated spectrum at $\mu_0 H_z = -14$ mT. Eigenmodes in (c) are subdivided in three groups d, m, and v. Black ticks refer to mode profiles and amplitudes displayed in (d) and (e), respectively. The size of the dots represents the amplitude. The color bar represents spin wave phase ranging from $-\pi$ to $+\pi$. (e) Spin-precessional amplitudes are plotted along **z** for a fixed position in the **x**-**y** plane of the NT.

v, respectively. In each group, a peak is selected (marked with a black tick at the bottom). The corresponding phase pattern and amplitude profile are displayed in Figs. 4(d) and 4(e), respectively. The amplitudes are extracted along a line in the z-direction. Vertical dashed lines indicate the width of the DW located near $z = 280$ nm. The simulated low-frequency resonance at 2 GHz (just below the BLS detection window) is attributed to a DW resonance with weak excitation outside (d-mode, supplemental movie11 [31]). At 6.6 GHz we find spin-precessional motion with nodes outside the DW (m-mode, supplemental movie12 [31]). This mode

thereby exhibits a nonzero k_z within the vortex region. The corresponding DE configuration explains the increased frequency. In the following, we select one specific example for a v-mode. At 8.6 GHz (supplemental movie13 [31]) we extract six clearly defined nodes along the NT, i.e., $m = 7$, giving rise to a large k_z. The corresponding wavelength amounts to 160 nm and is in the dipole-exchange regime of spin waves. Analyzing the phase profile in Fig. 4(d), we find that nodal lines at 8.6 GHz have again a chiral appearance, consistent with the predicted asymmetric spin-wave dispersion relations.

V. CONCLUSIONS AND REMARKS

In summary, we detected spin waves in permalloy nanotubes using microfocus BLS. The observed low-frequency resonances were in contrast to theoretical predictions for straight and infinitely long nanotubes. This discrepancy and the observation of unintentional nanotroughs in the real nanotubes motivated us to compare the detected spectra with simulations considering a nanotube segment with slanted edges. Based on the micromagnetic simulations, the rich experimental spectra of eigenmodes were then attributed to spin waves fulfilling interference conditions along both the azimuthal and axial directions of the NT. In the axial magnetic state, nodal lines were found to be mainly straight along the circumference. For helical and vortexlike magnetization orientations, however, nodal lines were distorted, which we attribute to the magnetochiral field predicted for nanometric ferromagnetic nanotubes. We hence observe an unusual nature of confined modes reminiscent of magnets subject to Dzyaloshinskii-Moriya interaction. Our findings pave the way for magnetochiral magnonics, which is based on 3D device architectures incorporating segments of nanotubular geometry with different magnetic states.

[1] V. V. Kruglyak, S. O. Demokritov, and D. Grundler, J. Phys. D **43**, 264001 (2010).

[2] K. Vogt, F. Fradin, J. Pearson, T. Sebastian, S. Bader, B. Hillebrands, A. Hoffmann, and H. Schultheiss, Nat. Commun. **5**, 3727 (2014).

[3] G. Gubbiotti, *Three-Dimensional Magnonics: Layered, Micro-and Nanostructures*, 1st ed. (Jenny Stanford Publishing, Singapore, 2019).

[4] S. Sahoo, A. May, A. van Den Berg, A. K. Mondal, S. Ladak, and A. Barman, Nano Lett. **21**, 4629 (2021).

[5] S. Sahoo, S. Mondal, G. Williams, A. May, S. Ladak, and A. Barman, Nanoscale **10**, 9981 (2018).

[6] S. S. P. Parkin, M. Hayashi, and L. Thomas, Science **320**, 190 (2008).

[7] P. Fischer, D. Sanz-Hernández, R. Streubel, and A. Fernández-Pacheco, APL Mater. **8**, 010701 (2020).

[8] R. Streubel, P. Fischer, F. Kronast, V. P. Kravchuk, D. D. Sheka, Y. Gaididei, O. G. Schmidt, and D. Makarov, J. Phys. D **49**, 363001 (2016).

[9] A. Fernández-Pacheco, R. Streubel, O. Fruchart, R. Hertel, P. Fischer, and R. P. Cowburn, Nat. Commun. **8**, 15756 (2017).

[10] H. Leblond and V. Veerakumar, Phys. Rev. B **70**, 134413 (2004).

[11] J. Escrig, J. Bachmann, J. Jing, M. Daub, D. Altbir, and K. Nielsch, Phys. Rev. B **77**, 214421 (2008).

[12] P. Landeros, O. J. Suarez, A. Cuchillo, and P. Vargas, Phys. Rev. B **79**, 024404 (2009).

[13] D. Rüffer, R. Huber, P. Berberich, S. Albert, E. Russo-Averchi, M. Heiss, J. Arbiol, A. Fontcuberta i Morral, and D. Grundler, Nanoscale **4**, 4989 (2012).

[14] M. M. Salazar-Cardona, L. Körber, H. Schultheiss, K. Lenz, A. Thomas, K. Nielsch, A. Kákay, and

J. A. Otálora, Appl. Phys. Lett. **118**, 262411 (2021).

[15] R. Hertel, SPIN **03**, 1340009 (2013).

[16] J. A. Otálora, M. Yan, H. Schultheiss, R. Hertel, and A. Kákay, Phys. Rev. Lett. **117**, 227203 (2016).

[17] J. A. Otálora, M. Yan, H. Schultheiss, R. Hertel, and A. Kákay, Phys. Rev. B **95**, 184415 (2017).

[18] M. Yang, B. Yin, Z. Li, X. Zeng, and M. Yan, Phys. Rev. B **103**, 094404 (2021).

[19] F. Balhorn, S. Jeni, W. Hansen, D. Heitmann, and S. Mendach, Appl. Phys. Lett. **100**, 222402 (2012).

[20] F. Balhorn, C. Bausch, S. Jeni, W. Hansen, D. Heitmann, and S. Mendach, Phys. Rev. B **88**, 054402 (2013).

[21] M. C. Giordano, K. Baumgaertl, S. Escobar Steinvall, J. Gay, M. Vuichard, A. Fontcuberta i Morral, and D. Grundler, ACS Appl. Mater. Interfaces **12**, 40443 (2020).

[22] M. C. Giordano, S. Escobar Steinvall, S. Watanabe, A. Fontcuberta i Morral, and D. Grundler, Nanoscale **13**, 13451 (2021).

[23] L. Körber, M. Zimmermann, S. Wintz, S. Finizio, M. Kronseder, D. Bougeard, F. Dirnberger, M. Weigand, J. Raabe, J. A. Otálora, H. Schultheiss, E. Josten, J. Lindner, I. Kézsmárki, C. H. Back, and A. Kákay, Phys. Rev. B **104**, 184429 (2021).

[24] L. Körber, I. Kézsmárki, and A. Kákay, Phys. Rev. B **105**, 184435 (2022).

[25] A. Mehlin, B. Gross, M. Wyss, T. Schefer, G. Tütüncüoglu, F. Heimbach, A. Fontcuberta i Morral, D. Grundler, and M. Poggio, Phys. Rev. B **97**, 134422 (2018).

[26] M. Wyss, A. Mehlin, B. Gross, A. Buchter, A. Farhan, M. Buzzi, A. Kleibert, G. Tütüncüoglu, F. Heimbach, A. Fontcuberta i Morral, D. Grundler, and M. Poggio, Phys. Rev. B **96**, 024423 (2017).

[27] A. V. Chumak, P. Kabos, M. Wu, C. Abert, C. Adelmann, A. O. Adeyeye, J. Åkerman, F. G. Aliev, A. Anane, A. Awad, C. H. Back, A. Barman, G. E. W. Bauer, M. Becherer, E. N. Beginin, V. A. S. V. Bittencourt, Y. M. Blanter, P. Bortolotti, I. Boventer, D. A. Bozhko *et al.*, IEEE Trans. Magn. **58**, 1 (2022).

[28] M. C. Giordano, Atomic layer deposition of Ni and $Ni_{80}Fe_{20}$ for tubular spin-wave nanocavities, Ph.D. thesis, EPFL, 2021, https://doi.org/10.5075/epfl-thesis-8372.

[29] B. W. Zingsem, M. Farle, R. L. Stamps, and R. E. Camley, Phys. Rev. B **99**, 214429 (2019).

[30] P. Che, I. Stasinopoulos, A. Mucchietto, J. Li, H. Berger, A. Bauer, C. Pfleiderer, and D. Grundler, Phys. Rev. Res. **3**, 033104 (2021).

[31] See Supplemental Material at http://link.aps.org/supplemental/10.1103/PhysRevMaterials.7.024405 for supplemental movies that (a) represent the spin-wave profile across a cross-sectional cut at the represented height of the NT, and (b) show the spin-wave profile on the entire NT while NT is rotating along its axis. The spin-wave amplitude is represented by the size of the dots. The color bar represents the spin-wave phase ranging from $-\pi$ to $+\pi$. The supplemental movies were prepared using Mayavi [39].

[32] F. Matteini, G. Tütüncüoglu, D. Mikulik, J. Vukajlovic-Plestina, H. Potts, J.-B. Leran, W. C. Carter, and A. Fontcuberta i Morral, Cryst. Growth Des. **16**, 5781 (2016).

[33] A. P. Chen, J. M. Gonzalez, and K. Y. Guslienko, J. Appl. Phys. **109**, 073923 (2011).

[34] D. Rüffer, M. Slot, R. Huber, T. Schwarze, F. Heimbach, G. Tütüncüoglu, F. Matteini, E. Russo-Averchi, A. Kovács, R. Dunin-Borkowski, R. R. Zamani, J. R. Morante, J. Arbiol, A. Fontcuberta i Morral, and D. Grundler, APL Mater. **2**, 076112 (2014).

[35] S. O. Demokritov and V. E. Demidov, IEEE Trans. Magn. **44**, 6 (2008).

[36] T. Sebastian, K. Schultheiss, B. Obry, B. Hillebrands, and H. Schultheiss, Front. Phys. **3**, 35 (2015).

[37] C. S. Davies, A. V. Sadovnikov, S. V. Grishin, Y. P. Sharaevskii, S. A. Nikitov, and V. V. Kruglyak, Appl. Phys. Lett. **107**, 162401 (2015).

[38] M. J. Donahue and D. G. Porter, OOMMF User's Guide, Version 1.0 (U.S. Department of Commerce, National Institute of Standards and Technology, 1999).

[39] P. Ramachandran and G. Varoquaux, Comput. Sci. Eng. **13**, 40 (2011).

[40] F. Crameri, Zenodo 10.5281/ZENODO.5501399.

[41] F. Crameri, G. E. Shephard, and P. J. Heron, Nat. Commun. **11**, 5444 (2020).

[42] I. Neudecker, K. Perzlmaier, F. Hoffmann, G. Woltersdorf, M. Buess, D. Weiss, and C. H. Back, Phys. Rev. B **73**, 134426 (2006).

[43] J. Podbielski, F. Giesen, and D. Grundler, Phys. Rev. Lett. **96**, 167207 (2006).

[44] S. Neusser, B. Botters, and D. Grundler, Phys. Rev. B **78**, 054406 (2008).

[45] J. Chen, H. Wang, T. Hula, C. Liu, S. Liu, T. Liu, H. Jia, Q. Song, C. Guo, Y. Zhang, J. Z. J. Zhang, X. Han, D. Yu, M. Wu, H. Schultheiss, and H. Yu, Nano Lett. **21**, 6237 (2021).

[46] D. Rueffer, Magnetic states and spin-wave modes in single ferromagnetic nanotubes, Ph.D. thesis, EPFL, 2014, https://doi.org/10.5075/epfl-thesis-6316.

[47] J. Jorzick, S. O. Demokritov, B. Hillebrands, M. Bailleul, C. Fermon, K. Y. Guslienko, A. N. Slavin, D. V. Berkov, and N. L. Gorn, Phys. Rev. Lett. **88**, 047204 (2002).

[48] A. G. Gurevich and G. A. Melkov, *Magnetization Oscillations and Waves* (CRC, Boca Raton, FL, 1996).